Characterization of the Plasma in a Hall Thruster †

E. Ahedo, P. Martínez Cerezo, and J.M. Gallardo
E.T.S.I. Aeronáuticos, Univ. Politécnica, 28040 Madrid, Spain

M. Martínez-Sánchez
Dep. of Aeronautics & Astronautics, M.I.T., Cambridge, MA 02139

IEPC-01-017

A model of the plasma axial discharge in a Hall thruster, which includes effects of both losses to dielectric walls and heat conduction is presented. The interaction of the plasma with dielectric walls is included through three frequencies accounting for ion recombination, energy losses, and near-wall-conductivity. These frequencies depend on the secondary emission of the dielectric walls and the dynamics of the radial plasma flow. Energy losses, concentrated in the acceleration region, reduce plasma temperatures, near-wall conductivity is marginal, and ion recombination is high in the diffusion region. The main effects of heat conduction are the smoothing on the temperature profile around the ionization region, and a strong restriction to the parametric range where efficient stationary solutions are found.

1 Introduction

In a recent paper we presented a 1-D macroscopic model of the stationary structure of the plasma flow in a SPT-type Hall thruster [1]. It includes the plasma response both inside the thruster channel and in the near-plume. The plasma in the plume is modeled as a 1-D jet of divergent area and includes a virtual-cathode surface to inject electrons and neutralize the ion beam. The matching of the plasma flows in channel and plume yields a complete picture of the plasma discharge in a Hall thruster and allows us to study the influence of design parameters on thruster performances.

The main flaw of the published model was the high temperatures found around the ionization layer. Heat conduction and losses to lateral dielectric walls, neglected in the model, are expected to be the mechanisms limiting the peaks of temperature.

The inclusion of a heat conduction law in the axial model of the plasma discharge, modifies the singular points of the mathematical model, and the integration procedure. Preliminary results were presented in Ref. [2].

The interaction with lateral walls leads to losses in plasma current, azimuthal momentum and internal energy, which can be included in a 1D axial model through three source terms. To estimate these terms requires to know the plasma response in each radial cross-section. Fife, Martínez-Sánchez, and Szabo [3], used a model of the space-charge sheath which accounted for secondary-emission, to determine the dependence of these terms on the plasma temperature and the wall material. Then, Jolivet and Roussel [4] pointed out that secondary emission could lead to charge saturation of the sheath. Recently, we presented a revised version of the model of Fife *et al.*, including a charge-saturated sheath regime and 'frictional' effects on the radial ion dynamics [5].

This paper presents an axial model which includes both heat conduction and interaction with lateral walls, with wall-source terms taken from Ref. [5]. However, results presented here are only for two partial models, each one taking into account only one of the above phenomena. Results including both effects simultaneously are still under research.

In Sec. 2 we present the complete equations and conditions of the new axial model. In Sec. 3 we discuss the effects of the plasma interaction with lateral walls. In Sec. 4 we present the solution with heat conduction. In Sec. 5 we summarize results and conclusions.

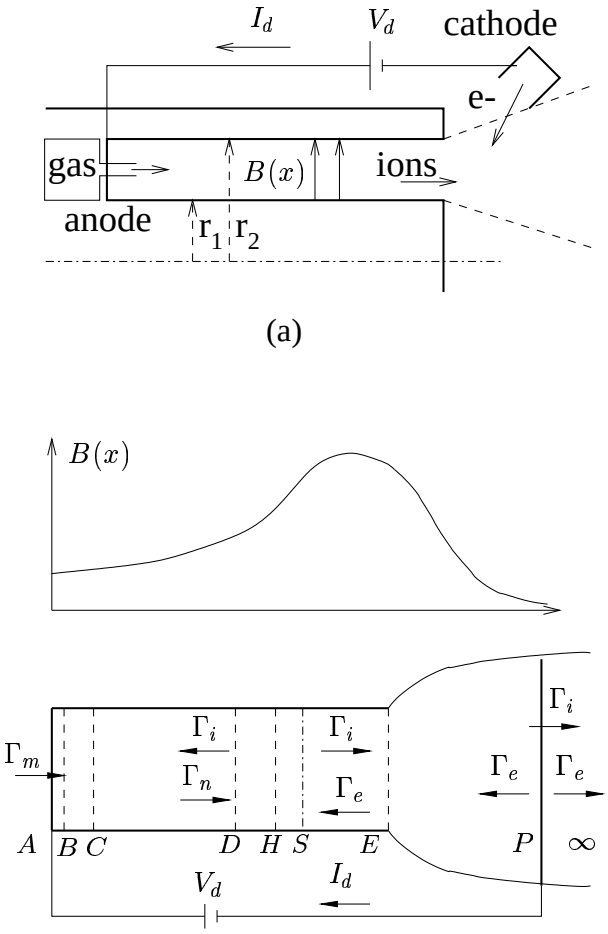

Figure 1.- Sketches of (a) the Hall thruster, and (b) the axial model. $\Gamma_\alpha = A_c n_\alpha v_{x\alpha}$, $\alpha = i, e, ...$ are axial flows of particles of the different species. The anode is A and surface P is the virtual cathode.

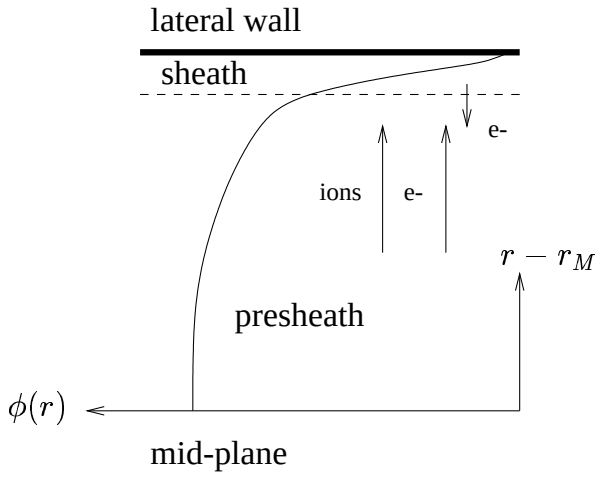

Figure 2.- Sketch of the radial model.

2 Model formulation

Geometrical sketches of the thruster and the axial and radial models are drawn in Figs. 1(a)-1(b) and Fig. 2. The main hypotheses of the axial model were discussed in detail in Refs. [1] and [5]. In the 1D axial model, plasma variables represent average values on each cross-section and depend only on the axial variable x. The axial profile of the radial magnetic field is assumed piece-wise Gaussian, B_m being its maximum value. The channel is of length L and radial area A_c. Electrons are injected into the plume at a neutralization surface (point P) placed at a distance L_{EP} from the channel exit (point E). The voltage difference between anode (point A) and point P is the discharge voltage, V_d, and the electron current delivered at the neutralization surface is the discharge current, I_d. One part of this current diffuses inwards across the magnetic field lines and ionizes the mass flow of neutrals, $\dot{m}$, injected at the anode. The other part flows outwards and neutralizes the ion current; subscript ∞ will refer to downstream conditions far away from the cathode.

In the axial model the plasma is considered quasineutral everywhere except in a thin electron-repelling sheath attached to the anode (region AB in Fig. 1(b), with $x_B \simeq x_A = 0$ in the quasineutral scale). The potential jump in the sheath, $\phi_{AB} = \phi_B - \phi_A > 0$, adjusts the small diffusive electron flow in the channel with the thermal flow collected at the anode. Since all ions are created by ionization within the thruster, plasma quasineutrality implies the back-flow of ions in the rear part of the channel.

The stationary, macroscopic equations for the quasineutral plasma between the entrance to the anode sheath (point B) and the external neutralization surface (point P) are

$$\frac{1}{A}\frac{d}{dx}(An_e v_{xi}) = \frac{1}{A}\frac{d}{dx}(An_e v_{xe}) = -\frac{1}{A}\frac{d}{dx}(An_n v_n) = n_e(\nu_i - \nu_w), \quad (1)$$

$$\frac{1}{A}\frac{d}{dx}(Am_i n_e v_{xi}^2) = -en_e\frac{d\phi}{dx} + m_i n_e(\nu_i v_n - \nu_w v_{xi}), \quad (2)$$

$$\frac{1}{A}\frac{d}{dx}(Am_i n_n v_n^2) = m_i n_e(\nu_w v_{nw} - \nu_i v_n), \quad (3)$$

$$0 = -\frac{d}{dx}n_e T_e + en_e\frac{d\phi}{dx} - \nu_d m_e n_e v_{xe}, \quad (4)$$

$$\frac{1}{A}\frac{d}{dx}A\left(\frac{3}{2}T_e n_e v_{xe} + q_{xe}\right) = -n_e T_e\frac{dv_{xe}}{dx} + \nu_d m_e n_e v_{xe}^2 - \nu_i n_e \alpha_i E_i - \nu_{we} n_e T_e, \quad (5)$$

$$\frac{dT_e}{dx} = -\frac{2m_e\nu_d}{5n_eT_e}q_{xe}, \tag{6}$$

For a complete listing of symbols and definitions see Ref. [1] and [5]. The ionization frequency follows

$$\nu_i = n_n R_i(T_e);$$

the axial diffusion frequency for the magnetized electrons satisfies

$$\nu_d = \frac{\omega_e^2}{\nu_e + \nu_{wm}}, \tag{7}$$

with

$$\nu_e = \nu_{en} + \nu_{ei} + \alpha_B\omega_e$$

the electron collision frequency, grouping contributions from $e-n$ and $e-i$ collisions, and Bohm anomalous diffusion; ν_w, ν_{wm} and ν_{we} are frequencies accounting for particle losses, near-wall conductivity, and energy losses at the lateral walls, to be defined below; v_{nw} is the axial velocity of ions after wall recombination and accommodation. The area $A(x)$ and thickness $d(x)$ of the plasma jet cylindrical cross-section, are constant within the channel and satisfy

$$\frac{d}{dx}\ln A = \frac{d}{dx}\ln d = \frac{2}{d}\tan\delta, \quad x > L \tag{8}$$

in the plume, with δ the local mean angle of divergence of each boundary, to be defined below.

The azimuthal components of the electron velocity and the heat flux follow

$$\frac{v_{\theta e}}{v_{xe}} \simeq \frac{q_{\theta e}}{q_{xe}} \simeq -\frac{\omega_e}{\nu_e}, \tag{9}$$

with $\omega_e/\nu_e \gg 1$.

2.1 Frequencies for lateral wall effects

They are determined from the radial model discussed in Ref. [5]. The particle loss frequency satisfies

$$\nu_w = \nu_0\tilde{\nu}_w \tag{10}$$

where

$$\nu_0 = \frac{\sqrt{T_e/m_i}}{d} \tag{11}$$

is the reference frequency for the radial motion, and $\tilde{\nu}_w$ is a dimensionless factor, which depends on the characteristics of the radial motion. In this paper we will just take the simplest case

$$\tilde{\nu}_w = \text{const.}$$

Future work will have to take into account the influence of the radial dynamics of ions and secondary electrons on $\tilde{\nu}_w$.

[In Ref. [5] we showed that, for the case of total trapping of secondary electrons, $\tilde{\nu}_w$ depends on frictional effects on the ion radial motion, which shape the profile of the radial presheath. This friction defines a frequency which can be approximated by

$$\nu_r \sim \nu_i + \frac{v_{xi}}{\sqrt{T_e}}\frac{\partial\sqrt{T_e}}{\partial x}, \tag{12}$$

and a dimensionless frequency parameter $\tilde{\nu}_r = \nu_r/\nu_0$. The function $\tilde{\nu}_w(\tilde{\nu}_r)$ is given by

$$\begin{aligned} \tilde{\nu}_r(\alpha) &= 2\Big(\frac{1+\alpha}{\sqrt{\alpha}}\arctan\sqrt{\alpha} - 1\Big), \\ \tilde{\nu}_w(\alpha) &= \frac{\tilde{\nu}_r(\alpha)}{\alpha}, \end{aligned} \tag{13}$$

where α is an intermediate parameter used for convenience.

The frequencies for near-wall diffusion and heat losses are

$$\begin{aligned} \nu_{wm} &= \beta_m\nu_w, \quad \beta_m(\delta_w) = \frac{\delta_w}{1-\delta_w}, \\ \nu_{we} &\simeq \beta_e\nu_w, \quad \beta_e(\delta_w) \sim 5.62 + \frac{1.65}{1-\delta_w}, \end{aligned} \tag{14}$$

with β_m and β_e enhancement functions, which depend on the effective secondary emission yield $\delta_w(T_e)$. Assuming that the secondary emission yield for an impinging monoenergetic electron beam of energy E, follows the law

$$\bar{\delta}_w(E) \simeq \sqrt{E/\bar{E}_w},$$

the effective yield for the quasi-Maxwellian population of primary electrons, satisfies

$$\delta_w(T_e) \simeq \min\Big\{\delta_w^*, \sqrt{\frac{T_e}{E_w}}\Big\}, \tag{15}$$

with

$$E_w \sim \frac{2}{3}\bar{E}_w$$

the temperature leading hypothetically to 100% secondary emission [5] and

$$\delta_w^* \simeq 0.983$$

the upper-bound value of δ_w, corresponding to the charge-saturated regime for the lateral sheaths. Therefore, the maximum values of the enhancement functions are

$$\beta_m^* \sim 60,\ \beta_e^* \sim 105,$$

and the charge-saturation regime corresponds to $T_e \geq 0.967E_w$.

3 Solution with wall losses

Here we take $q_{xe} = 0$ in Eq. (5) and we avoid Eq. (6). Solving Eqs. (1)-(5) for the spatial derivatives we obtain a matrix relation of the form

$$(1 - M^2)\frac{d\boldsymbol{Y}}{dx} = \boldsymbol{F}(\boldsymbol{Y}), \tag{16}$$

where $\boldsymbol{Y} = (T_e, n_e, n_n, v_{xi}, v_{xe}, v_n, \phi)$ groups the 7 plasma variables, $\boldsymbol{F}$ is a regular function and

$$M = \frac{v_{xi}}{\sqrt{5T_e/3m_i}} \tag{17}$$

is the Mach number for the ion axial flow. For instance, the equation for v_{xi} can be written as

$$\frac{dv_{xi}}{dx} = \nu_i - \nu_w - v_{xi}\Big(\frac{G}{P} + \frac{1}{A}\frac{dA}{dx}\Big) \tag{18}$$

with

$$P = T_e(1 - M^2) \tag{19}$$

and

$$\begin{aligned} v_{xe}G = \nu_i\Big[\frac{2}{5}\alpha_i E_i + T_e - \frac{3}{5}m_i(2v_{xi} - v_n)v_{xe}\Big] \\ - \nu_d m_e v_{xe}^2 + \frac{3}{5}m_i v_{xi}^2 v_{xe}\frac{d\ln A}{dx} \\ + \frac{2}{5}\nu_{we}T_e - \Big(T_e - \frac{3}{5}m_i v_{xi}v_{xe}\Big)\nu_w. \end{aligned} \tag{20}$$

Sonic points and boundary conditions are discussed in Ref. [1]. The seven boundary conditions needed here are:

i)-ii) The injected flow of neutrals at the anode, $\dot{m}$, and their velocity, $v_{nB} = v_{nA}$, are known.

iii) The electron temperature at the neutralization surface, T_{eP}, is known.

iv) The potential drop between points A and P is the discharge voltage, $\phi_A - \phi_P = V_d$.

v) The presheath/sheath transition at point B requires $M_B = -1$, which is the Bohm sonic condition on the ion back-flow.

vi) The potential jump at the anode sheath satisfies

$$\frac{e\phi_{AB}}{T_{eB}} = \ln\frac{\bar{c}_{eB}}{4|v_{xeB}|} > 0, \tag{21}$$

with $\bar{c}_e = \sqrt{8T_e/\pi m_e}$.

vii) There is a regular sonic point inside the channel (point S), which, according to Eq.(18), is characterized by

$$G_S = 0 \text{ at } M_S = 1 \tag{22}$$

In addition, we must define an expression for the angle of divergence δ. Following Ref. [1] we take

$$\tan\delta = \frac{\sqrt{5T_{eE}/3m_i}}{v_{xi}} \tag{23}$$

Notice that discharge current, I_d, position of forward sonic point, x_S, and divergence angle at the channel exit, δ_E, are part of the solution.

3.1 Axial plasma structure

Figure 3 shows the first complete results we have obtained with the preceding model of radial losses. Profiles of most plasma variables are shown for a SPT-100 type of thruster. The solution shown here presents moderate wall losses. However, the values selected for the parameters that determine radial losses: $\tilde{\nu}_w \sim 0.17$ and $E_w = 100eV$, were aimed mainly to test the possibility of obtaining valid solutions. Our procedure to obtain these solutions is to carry out a parametric continuation from the solution without wall losses $\nu_w = 0$. Actual values of E_w for BN-based materials are in the range $E_w \sim 2\bar{E}_w/3 \sim$ 15-40 eV. From Eq.(13) $\tilde{\nu}_w \sim 0.17$ corresponds to $\tilde{\nu}_r \simeq 50$, and $\nu_r \sim 10^7$Hz, which, from the definition of Eq.(12), seems too large; however, partial trapping, not investigated yet, could reduce $\tilde{\nu}_w$. Attempts to increase $\tilde{\nu}_w$ and reduce E_w, beyond the case of Fig. 3, have encountered different convergence difficulties. One of them is the appearance of complex values for the plasma derivatives at point S preventing the launch of the integration.

The solution of Fig. 3 shows that energy losses at lateral walls smooth the temperature profile, the maximum temperature decreasing from about 90 eV with no wall losses, to about 68 eV now, which corresponds to a maximum secondary yield of $\delta_w \sim 0.82$, far (in terms of losses) from the charge-saturation value δ_w^*. Energy losses take place in the acceleration region, where T_e is high. On the contrary, losses in plasma current are concentrated in the rear part of the channel. The (relative) ion back-flow at the inner boundary of the ionization layer is $\eta_{iD} \simeq -0.37$, whereas at the anode, it is just $\eta_{iB} \simeq -0.05$, which means a current loss in the diffusion region of 1.2 A. The total plasma current deposited at lateral walls, $\int S_w dx$, with

$$S_w = en_e\nu_w A_c$$

plotted in Fig. 3, is 2.0 A, about a 38% of the discharge current, $I_d = 5.21$ A, and a 34% of the total ion production (about 5.8 A); Bishaev and Kim [6] estimated relative current losses of similar magnitude in their experiments.

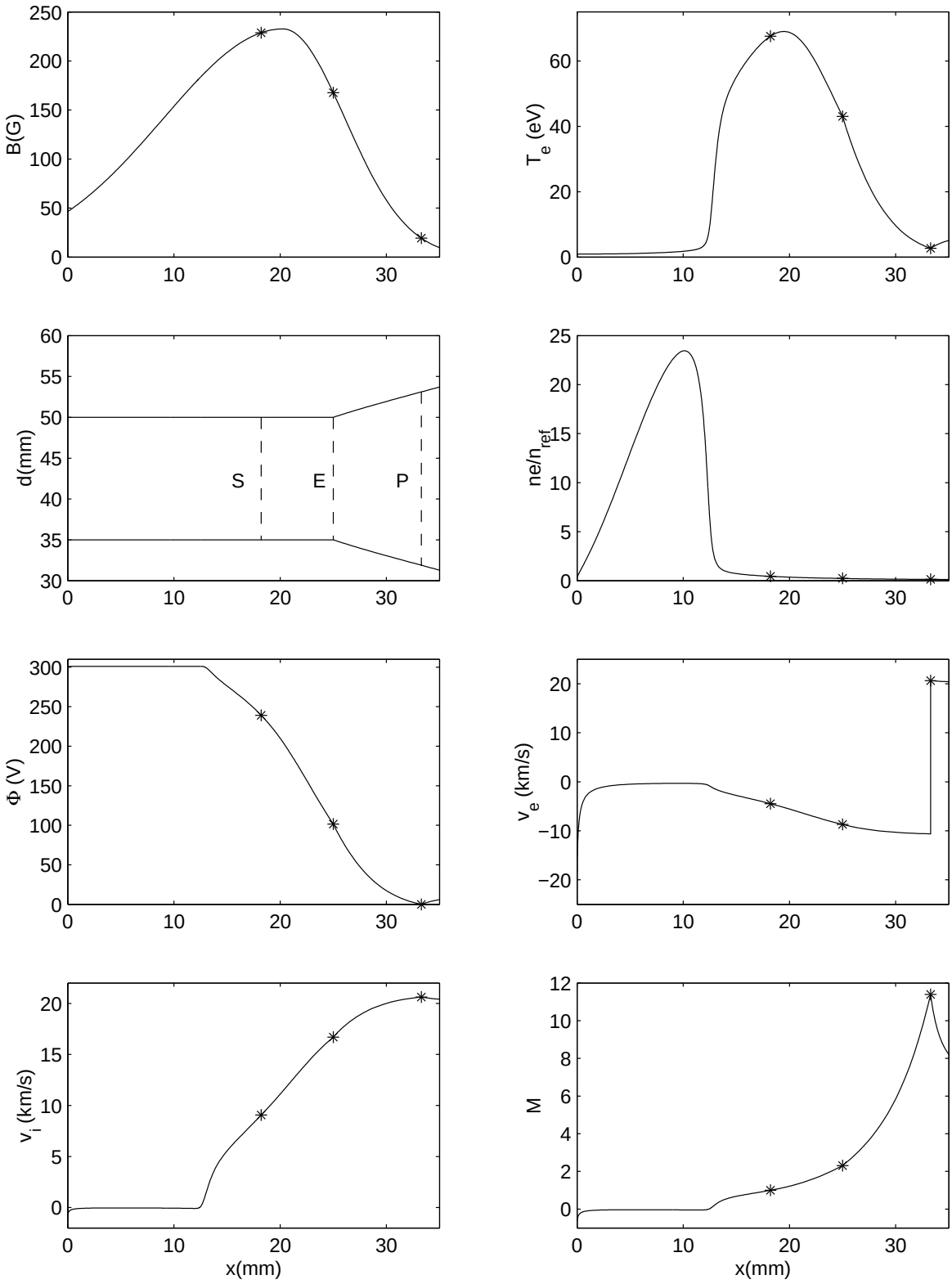

Figure 3 (continues in next page)

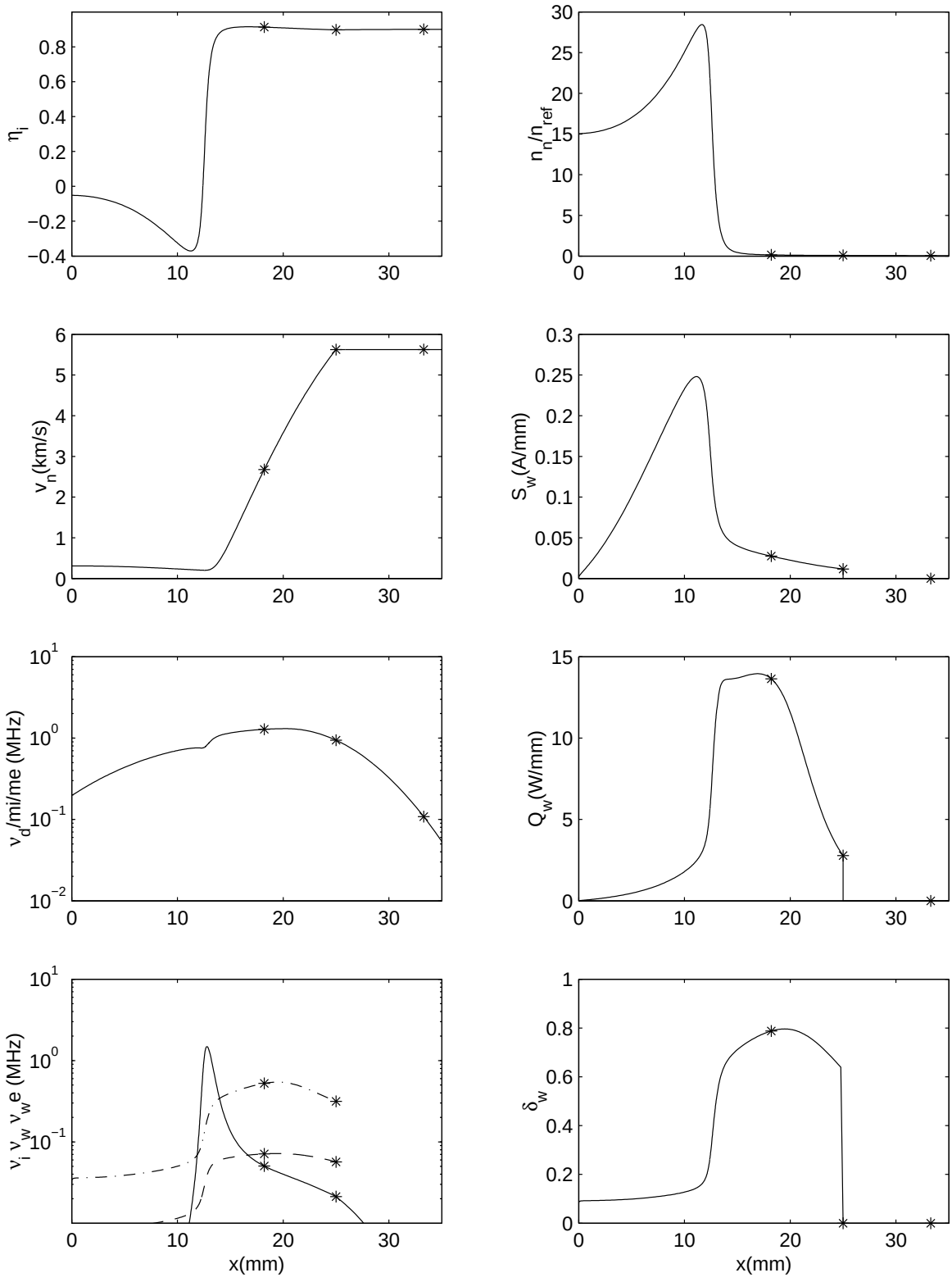

Figure 3(cont.).- Model with lateral losses (no heat conduction). Axial structure of the plasma discharge for $L = 25$mm, $L_{EP} = 8.3$mm, $A_c = 40.1$cm^2, $V_d = 300$V, $\dot{m} = 5.2$mg/s, $T_{eP} = 2.7$eV, $16\alpha_B \sim 0.21$, $E_w = 100$eV, $\tilde{\nu}_w(x) \sim 0.17$, $v_{nw} = v_i$, and $n_{ref} \simeq 4.3 \cdot 10^{18}$m^{-3}.

The electron energy deposited by conduction at lateral walls, $\int Q_w dx$, with

$$Q_w = T_e n_e \nu_{we} A_c$$

plotted in Fig. 3, is 144 W, which represents 9% of the electric power, $I_d V_d \simeq 1.56$ kW; Ref. [6] estimates this energy loss around 20%.

The structure of the plasma discharge in Fig. 3 is similar to the one discussed in Ref. [1] and sketched in Fig. 1(b). It consists of anode sheath (AB), anode presheath(BC), diffusion region(CD), ionization layer(DH), acceleration region(HE) and near-plume (EP). Delimiting points inside the channel are $x_A = 0$, $x_C \simeq 0.5$ mm, $x_D \simeq 11.5$ mm, $x_H \simeq 14$ mm. The regular sonic point is downstream of the ionization layer, at $x_S \simeq 18.2$ mm. Notice in Eq.(20) for G that the presence of two terms for lateral losses gives more flexibility to the balance necessary for a smooth sonic transition (i.e. $G_S = 0$). The drift of point S away from the ionization layer, when lateral losses are included, indicates that electron diffusion (i.e. Joule heating) and lateral energy losses dominate the balance at the sonic transition, that is we have

$$\frac{2}{5}\nu_{we} T_e \sim \nu_d m_e v_{xe}^2$$

at point S. In the acceleration region, volume ionization and ion recombination at lateral walls are rather low, keeping the ionization fraction $\eta_i(x)$ almost constant.

Potential drops in the different plasma regions are $\phi_{AB} \simeq 1.2$ V, $\phi_{CD} \simeq 0.02$ V, $\phi_{DS} \simeq -61.9$ V, $\phi_{SE} \simeq -137.6$ V, $\phi_{EP} \simeq -101.5$ V, $\phi_{P\infty} \simeq 10$ V. Notice that the potential drop in the ionization layer is moderate and follows the law [1] $\phi_{DH} \sim \frac{5}{6} T_{eH}$.

The thrust, defined as

$$F = (m_i n_i v_i^2 + p_e)_E A_c,$$

is $F = 90.6$ mN and the thrust efficiency (using the definition of Ref. [1]) is $\eta \simeq 0.50$, which comes from the product of utilization efficiency $\eta_u \simeq 0.90$, (electric) current efficiency $\eta_c \simeq 0.73$, energy efficiency $\eta_e \simeq 0.97$, and plume efficiency $\eta_p \simeq 0.86$.

4 Solution with heat conduction

Here we include Eq.(6) for q_{xe}, but we omit losses to lateral walls (i.e. we take $\tilde{\nu}_w = 0$). Heat conduction is not just another effect included into the zero-conduction model. It leads to a different mathematical model, with an extra differential equation and different singular points. This new model cannot be solved from parametric continuation on the zero-conduction model and requires a specific integration procedure.

Solving Eqs. (1)-(6) for the spatial derivatives we obtain again a relation of the form (16), but now

$$\boldsymbol{Y} = (q_{xe}, T_e, n_e, n_n, v_{xi}, v_{xe}, v_n, \phi)$$

groups 8 plasma variables,

$$M = \frac{v_{xi}}{\sqrt{T_e/m_i}} \tag{24}$$

is the isothermal Mach number, and function $\boldsymbol{F}$ is different from the no-conduction model. For instance, the ion velocity follows Eq.(18) but now the function G is

$$G = -\nu_d \Big[m_e v_{xe} - \frac{2 m_e q_{xe}}{5 n_e T_e} \Big] - \nu_i m_i (2 v_{xi} - v_n) + m_i v_{xi}^2 \frac{d \ln A}{dx}. \tag{25}$$

The eight boundary conditions for this model are the seven ones of the no-conduction model plus a condition for the heat flow deposited by the electrons into the anode sheath (at point B). From the analysis of the anode sheath, we find [2]

$$q_{xeB} = n_e v_{xe} T_e \big(\ln \frac{\bar{c}_e}{4|v_{xe}|} - \frac{1}{2} \big) \Big|_B. \tag{26}$$

Details about the way to integrate the differential equations are given in Ref. [2]. One new feature of the conduction model is the restriction of the relative ion back-flow, η_{iB}, to a narrow range. The matching of the quasineutral solution with the anode sheath requires (i) the anode sheath to be ion-attracting and (ii) the ion back-flow to accelerate towards the anode. The first condition means $\phi_{AB} > 0$. From Eq.(18), the second condition implies that $G_B > 0$, or, using Eq.(25) with $\nu_i \simeq 0$,

$$\frac{2 q_{xe}}{5 n_e T_e v_{xe}} \Big|_B < 1. \tag{27}$$

Using now Eqs. (21) and (26), the two conditions yield the double restriction

$$0 < \ln \frac{\bar{c}_{e_B}}{4|v_{xeB}|} < 3, \tag{28}$$

or, in terms of the ion back current,

$$5 \cdot 10^{-3} < |I_{iB}|/I_d < 0.114, \tag{29}$$

with $I_i = e n_i v_{xi} A_c$. However, difficulties found in the numerical convergence around point B near the limit $\phi_{AB} = 0$, have forced us to exchange that limit for the close one, $q_{xeB} = 0$, where $e\phi_{AB}/T_{eB} = 0.5$. This moves the lower bound of the ion back-current to $|I_{iB}|/I_d \sim 8 \cdot 10^{-3}$.

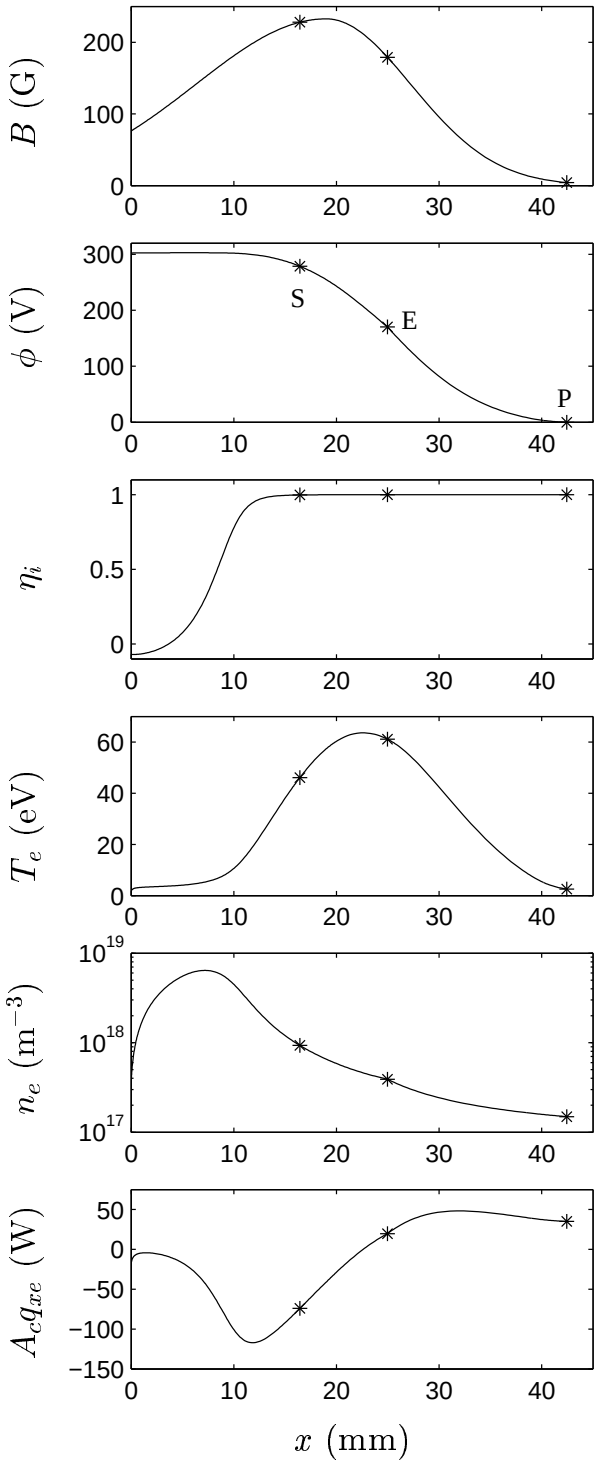

Figure 4.- Model with heat conduction (and no wall losses). Axial structure of the plasma discharge for: $L = 25$mm, $L_{EP} = 21.1$mm, $A_c = 45$cm^2, $V_d = 300$V, $\dot{m} = 5.2$mg/s, $T_{eP} = 2.5$eV, $16\alpha_B \sim 0.067$.

4.1 Axial plasma structure

Figure 4 shows the axial profiles of main plasma variables for an SPT-100 type of thruster. Design and control parameters are similar to the case of Fig. 3. The plasma structure presents similar trends to the no-conduction solution of Ref. [1] (with no lateral losses). Heat conduction smoothes the temperature profile in two ways: first, the peak temperature is reduced from about 90 eV to 65 eV; second there is a smoother transition between the diffusion and ionization regions, leading to a shorter diffusion region, and a larger ionization layer.

Plasma equations and boundary conditions seem to force an almost monotonic profile of q_{xe} between B and S. As a consequence, q_{xeS} cannot be close to zero, moving the point of maximum temperature (i.e., $q_{xe} = 0$) away from point S and closer to the channel exit. Actually we could not find good solutions with the point of maximum temperature well inside the channel. From Eq.(25), a regular sonic transition, in the present model, implies balancing Joule heating, conductive heat flow, and ionization losses. The large value of q_{xeS} implies that this balance takes place mainly between heat conduction and Joule heating,

$$q_{xe} \sim \frac{5}{2} n_e T_e v_{xe},$$

placing point S outside the ionization layer.

For the case of Fig. 4, Fig. 5(a)-(c) measure different phenomena in the electron dynamics. This is aimed at evaluating the validity of the hypotheses supporting our model. Figure 5(a) shows the different contributions to the total collision frequency of electrons, Eq.(2). Bohm diffusion provides the main contribution from the ionization layer towards the exit, whereas e-i collisions (instead of the e-n collisions) dominate in the diffusion region. This last feature is justified by the high plasma density and low temperature there, and needs further investigation. Figure 5(b) shows the axial profiles of the ionization frequency, with its peak marking the ionization region, and the effective axial frequency for electron diffusion, Eq.(134); the dominance of Bohm diffusion makes $\nu_d \propto B(x)$, approximately, in most of the channel. Figure 5(c) shows that the electron mean azimuthal energy (main contribution to the electron mean kinetic energy) is totally negligible compared to the thermal energy, except perhaps within a small region near the anode.

4.2 Thruster performance

Performance parameters for the case plotted in Fig. 4 are: $F \simeq 90.6$mN, $I_d \simeq 4.51$A ($i_d = 1.17$), and $\eta \simeq 57.5\%$.

The influence of the plasma discharge V_d and the magnetic field B_m on thruster performance have been computed from parametric continuation of the solution of Fig. 4. The consequence of the narrow interval for η_{iB} in Eq.(29), is a narrow range too for the control parameters where our model yields stationary solutions (with large ionization). As an example, Fig. 6(a) shows the narrow band for the pair of parameters (V_d, B_m), only a variation of about 10% is acceptable. Figures 6(b)-6(d) plot the corresponding bands for thrust, discharge current, and efficiency; for F, the band reduces practically to a line. These plots show that larger thrust and efficiency are obtained with larger V_d and B_m.

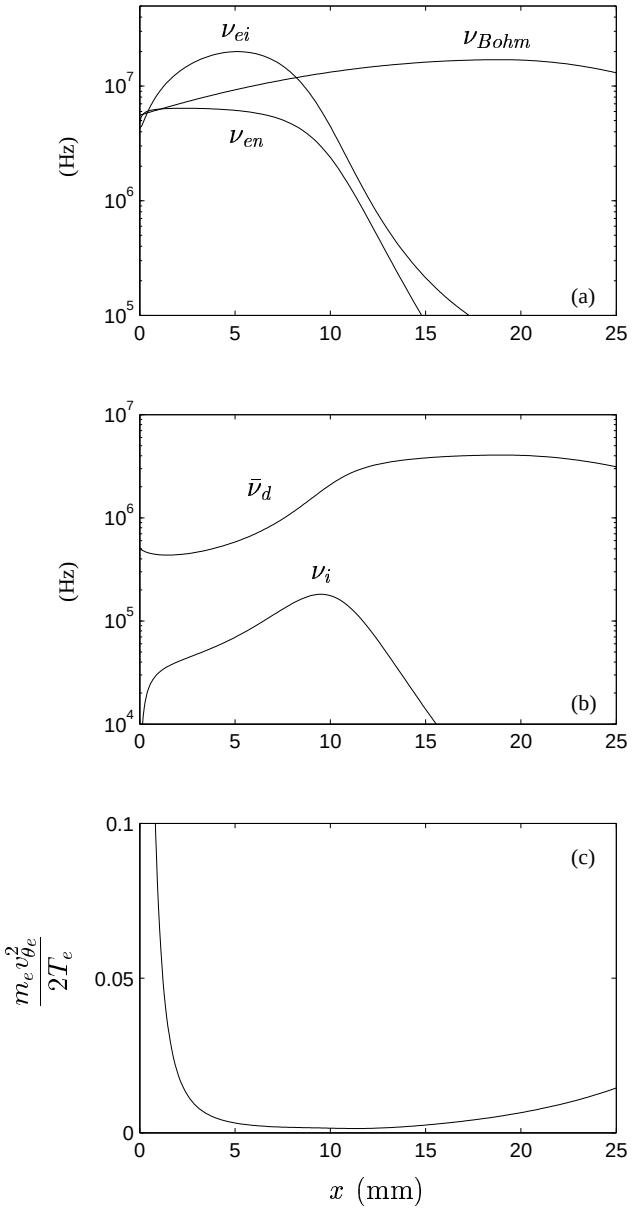

Figure 5.- Model with heat conduction (and no wall losses). Same case of Fig. 5. (a) Contributions of different processes to the electron collision frequency ν_e. (b) Axial diffusion frequency ($\bar{\nu}_d = \nu_d\sqrt{m_e/m_i}$) and ionization frequency along the channel. (c) Ratio of electron mean azimuthal kinetic energy to electron temperature.

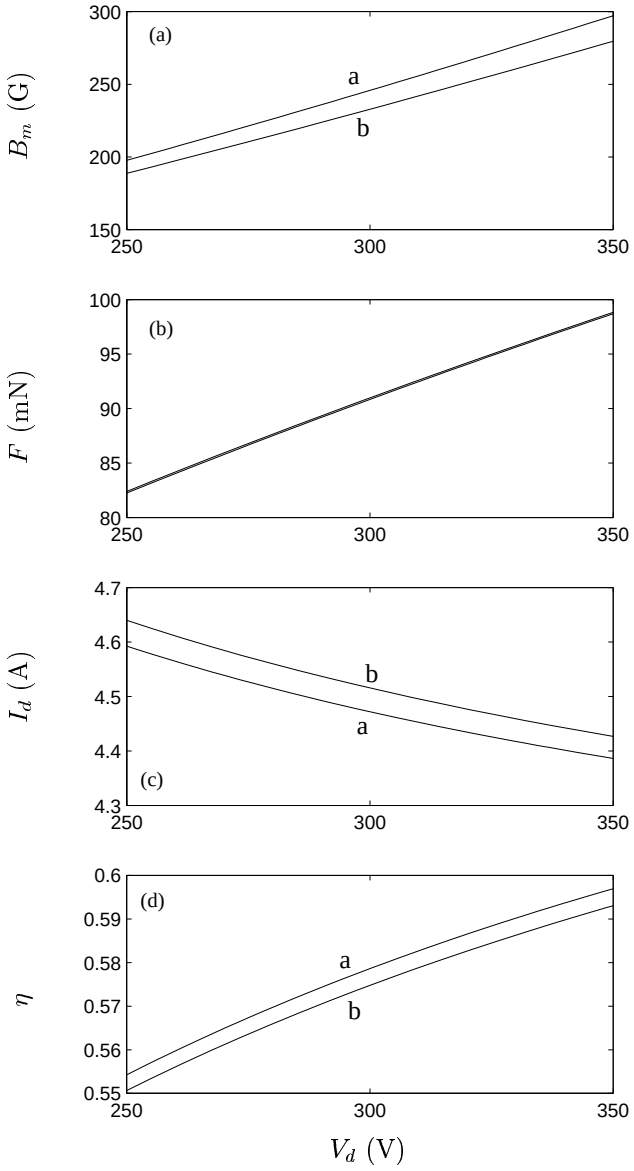

Figure 6.- Model with heat conduction (and no wall losses). (a) Band of input parameters (V_d, B_m) where stationary solutions have been found; rest of parameters as in Fig. 4. Line 'a' corresponds to $G_B = 0$, and line 'b' to $\phi_{AB} = 0$. Bands for (b) thrust, (c) discharge current, and (d) efficiency, corresponding to the (V_d, B_m) band.

5 Conclusions

We have presented a complete macroscopic model for the plasma axial discharge, with inclusion of terms for heat conduction and interaction with dielectric walls. Then, we have studied these two effects separately.

Solutions with lateral losses (and no heat conduction) have been found for $\tilde{\nu}_w$ well below one, which implies a strong inhibition of the plasma radial flow, necessary to have moderate wall losses. Our recent radial model (with total trapping of secondary electrons) proposed axial transport or collisions as possible inhibition mechanisms, but these two phenomena seem insufficient to reduce $\tilde{\nu}_w$ enough; partial trapping is the main mechanism remaining to be investigated. Energy losses, concentrated in the acceleration region, smooth the temperature profile. Particle losses to lateral walls in the diffusion region, imply a larger ion production in the ionization layer and eventually a larger discharge current, thus decreasing the thrust efficiency. Attempts to obtain solutions with larger lateral losses have found numerical difficulties which need to be interpreted.

Solutions with heat conduction (and no wall effects) keep the main trends of the basic non-conduction model, but the temperature profile is smoothed. In particular, heat conduction reduces the maximum temperature by one third, following now a law $T_{e,max} \sim \frac{1}{5} V_d$, roughly. This reduction of the maximum temperature is not enough to agree with experimental values (which are $T_{e,max} \sim 20 - 30eV$ for $V_d = 300$ V), implying that wall losses are still needed. Heat conduction spreads the ionization region, reduces the diffusion region, and places the sonic point downstream the ionization layer, and the maximum temperature close to the channel exit. A very significant feature of the conduction model is the restriction of the ion back current near the anode to a narrow range, below 15%, roughly, of the mass flow. Although these values agree with experimental evidence regarding the range for efficient thruster operation, the model shows a drastic reduction of the parametric range where stationary solutions with high-ionization efficiency are found.

Acknowledgments

The work at UPM was sponsored by research contract F61775-00-WE034 from the Air Force Office of Scientific Research's European Office for Aerospace Research and Development (EOARD). The project manager was Major Tim Lawrence, who was in charge of Space Technology. Also, E. Ahedo thanks the support of the Dirección General de Enseñanza Superior e Investigación Científica of Spain, under project PB97-0574-C04-02.

References

[1] E. Ahedo, P. Martínez-Cerezo, and M. Martínez-Sánchez. One-dimensional model of the plasma flow in a Hall thruster. *Physics of Plasmas*, 8:3058–3068, 2001.

[2] E. Ahedo, P. Martínez-Cerezo, J.M. Gallardo, and M. Martínez-Sánchez. Modelling the plasma flow in a hall thruster. In *7th Spacecraft Charging Technology, Noodrwijk, The Netherlands*, Noordwijk, The Netherlands, 2001. European Space Agency.

[3] J.M. Fife, M. Martínez-Sánchez, and J. Szabo. A Numerical Study of Low-Frequency Discharge Oscillations in Hall Thrusters. In *33rd Joint Propulsion Conference, Seattle, WA*, AIAA Paper No. 97-3052. American Institute of Aeronautics and Astronautics,Washington, DC, 1997.

[4] L. Jolivet and J.-F. Roussel. Effects of the secondary electron emission on the sheath phenomenon in a Hall thruster. In *3rd Int. Conference on Spacecraft propulsion, Cannes*. ESA/CNES, 2000.

[5] E. Ahedo, P. Martínez-Cerezo, and M. Martínez-Sánchez. Model of plasma-wall interaction effects in a hall thruster. In *37th Joint Propulsion Conference, Salt Lake City, UT*, AIAA Paper No. 2001-3323. American Institute of Aeronautics and Astronautics,Washington, DC, 2001.

[6] A.M. Bishaev and V. Kim. Local plasma properties in a Hall-current accelerator with and extended acceleration zone. *Sov. Physics-Tech. Physics*, 23(9):1055–1057, 1978.